


The production of ionizing photons in UV-faint $z \sim 3-7$ galaxies[★]

Gonzalo Prieto-Lyon^{1,2} , Victoria Strait^{1,2}, Charlotte A. Mason^{1,2}, Gabriel Brammer^{1,2}, Gabriel B. Caminha^{3,4}, Amata Mercurio^{5,6}, Ana Acebron^{7,8}, Pietro Bergamini^{7,9}, Claudio Grillo^{7,8}, Piero Rosati^{9,10}, Eros Vanzella¹⁰, Marco Castellano¹¹, Emiliano Merlin¹¹, Diego Paris¹¹, Kristan Boyett^{12,13}, Antonello Calabrò¹¹, Takahiro Morishita¹⁴, Sara Mascia¹¹, Laura Pentericci¹¹, Guido Roberts-Borsani¹⁵, Namrata Roy¹⁶, Tommaso Treu¹⁵, and Benedetta Vulcani¹⁷

¹ Cosmic Dawn Center (DAWN), Copenhagen, Denmark

² Niels Bohr Institute, University of Copenhagen, Jagtvej 128, 2200 Copenhagen N, Denmark
e-mail: gonzalo.prieto@nbi.ku.dk

³ Technische Universität München, Physik-Department, James-Frank-Str. 1, 85748 Garching, Germany

⁴ Max-Planck-Institut für Astrophysik, Karl-Schwarzschild-Str. 1, 85748 Garching, Germany

⁵ Dipartimento di Fisica “E.R. Caianiello”, Università Degli Studi di Salerno, Via Giovanni Paolo II, 84084 Fisciano, (SA), Italy

⁶ INAF – Osservatorio Astronomico di Capodimonte, Via Moiariello 16, 80131 Napoli, Italy

⁷ Dipartimento di Fisica, Università degli Studi di Milano, Via Celoria 16, 20133 Milano, Italy

⁸ INAF – IASF Milano, Via A. Corti 12, 20133 Milano, Italy

⁹ INAF – OAS, Osservatorio di Astrofisica e Scienza dello Spazio di Bologna, Via Gobetti 93/3, 40129 Bologna, Italy

¹⁰ Dipartimento di Fisica e Scienze della Terra, Università di Ferrara, Via Saragat 1, 44122 Ferrara, Italy

¹¹ INAF – Osservatorio Astronomico di Roma, Via Frascati 33, 00078 Monteporzio Catone, Rome, Italy

¹² School of Physics, University of Melbourne, Parkville 3010, VIC, Australia

¹³ ARC Centre of Excellence for All Sky Astrophysics in 3 Dimensions (ASTRO 3D), Mount Stromlo Rd, Australia

¹⁴ IPAC, California Institute of Technology, MC 314-6, 1200 E. California Boulevard, Pasadena, CA 91125, USA

¹⁵ Department of Physics and Astronomy, University of California, Los Angeles, 430 Portola Plaza, Los Angeles, CA 90095, USA

¹⁶ Center for Astrophysical Sciences, Department of Physics & Astronomy, Johns Hopkins University, Baltimore, MD 21218, USA

¹⁷ INAF – Osservatorio Astronomico di Padova, vicolo dell’Osservatorio 5, 35122 Padova, Italy

Received 22 November 2022 / Accepted 23 January 2023

ABSTRACT

Aims. The demographics of the production and escape of ionizing photons from UV-faint early galaxies is a key unknown that has hindered attempts to discover the primary drivers of reionization. With the advent of JWST, it is finally possible to observe the rest-frame optical nebular emission from individual sub- L^* $z > 3$ galaxies to measure the production rate of ionizing photons, ξ_{ion} .

Methods. Here we study a sample of 370 $z \sim 3-7$ galaxies spanning $-23 < M_{\text{UV}} < -15.5$ (median $M_{\text{UV}} \approx -18$) with deep multiband HST and JWST/NIRCam photometry that covers the rest-UV to the optical from the GLASS and UNCOVER JWST surveys. Our sample includes 102 galaxies with Lyman-alpha emission detected in MUSE spectroscopy. We used $H\alpha$ fluxes inferred from NIRCam photometry to estimate the production rate of ionizing photons that do not escape these galaxies, $\xi_{\text{ion}}(1 - f_{\text{esc}})$.

Results. We find median $\log_{10} \xi_{\text{ion}}(1 - f_{\text{esc}}) = 25.33 \pm 0.47$, with a broad intrinsic scatter of 0.42 dex, which implies a broad range of galaxy properties and ages in our UV-faint sample. Galaxies detected with Lyman-alpha have ~ 0.1 dex higher $\xi_{\text{ion}}(1 - f_{\text{esc}})$, which is explained by their higher $H\alpha$ equivalent width distribution; this implies younger ages and higher specific star formation rates and, thus, more O/B stars. We find significant trends of increasing $\xi_{\text{ion}}(1 - f_{\text{esc}})$ with increasing $H\alpha$ equivalent width, decreasing UV luminosity, and decreasing UV slope; this implies that the production of ionizing photons is enhanced in young galaxies with assumed low metallicities. We find no significant evidence for sources with very high ionizing escape fractions ($f_{\text{esc}} > 0.5$) in our sample based on their photometric properties, even amongst the Lyman-alpha-selected galaxies.

Conclusions. This work demonstrates that considering the full distribution of ξ_{ion} across galaxy properties is important for assessing the primary drivers of reionization.

Key words. quasars: emission lines – galaxies: high-redshift – galaxies: evolution

1. Introduction

In recent years, we have obtained increasing evidence that the reionization of hydrogen happened fairly late, approximately one billion years after the Big Bang ($z \sim 5.5-10$), with a mid-point around $z \sim 7-8$ (e.g., Fan et al. 2006; Stark et al. 2010; McGreer et al. 2015; Mason et al. 2018; Davies et al. 2018;

Qin et al. 2021; Planck Collaboration VI 2020; Bolan et al. 2022). However, there is evidence for significant star formation before this time (e.g., Oesch et al. 2018; Hashimoto et al. 2018; McLeod et al. 2021), and thus it appears that reionization lags behind galaxy formation. The reason for this lag is unknown: we are still lacking a full physical understanding of the reionization process. In particular, we still do not know which types of galaxies drive the process, that is to say, which physical mechanisms mediate the production and escape of ionizing photons from galaxies. In order to produce such a late and

* Catalogue is only available at the CDS via anonymous ftp to cdsarc.cds.unistra.fr (130.79.128.5) or via <https://cdsarc.cds.unistra.fr/viz-bin/cat/J/A+A/672/A186>

fairly rapid reionization, the ionizing population could have been dominated by low mass, UV-faint galaxies with a low average escape fraction ($\sim 5\%$; e.g., Mason et al. 2019; Qin et al. 2021). Alternatively, rarer, more massive galaxies with higher escape fractions could have been responsible (e.g., Sharma et al. 2017; Naidu et al. 2020). With only measurements of the timing of reionization, these scenarios are degenerate, and thus physical priors on the ionizing properties of galaxies across cosmic time are necessary to pinpoint the sources of reionization.

The total ionizing output of galaxies can be simply parameterized (e.g., Madau et al. 1999; Robertson et al. 2010) as the product of the production rate of ionizing photons relative to non-ionizing UV photons, ξ_{ion} (determined by the stellar populations; e.g., Stanway et al. 2016) and the fraction of ionizing photons that escape the interstellar medium (ISM) into the intergalactic medium, f_{esc} (determined by the structure and ionization state of the ISM, which is likely shaped by star formation and feedback; e.g., Trebitsch et al. 2017; Ma et al. 2020). Both of these quantities are also expected to vary with time in an individual galaxy, for example due to the lifetime and properties of young stellar populations, and depending on the effects of feedback and bursty star formation on the ISM.

While we can easily observe the non-ionizing UV photons from galaxies, the high optical depth of the intergalactic medium to ionizing photons makes direct measurements of the escaping ionizing spectrum statistically unlikely at $z \gtrsim 3$ (Inoue et al. 2014; Becker et al. 2021; Vanzella et al. 2018). Alternatively, fluxes of nonresonant recombination lines, emitted by gas that was ionized in HII regions around massive stars, can crucially measure the flux of ionizing photons that do not escape galaxies. In particular, $H\alpha$ emission can be used to directly estimate $(1 - f_{\text{esc}})\xi_{\text{ion}}$ (e.g., Leitherer & Heckman 1995; Bouwens et al. 2016; Shivaei et al. 2018; Emami et al. 2020). As f_{esc} is inferred to be low ($\lesssim 10\%$) on average for Lyman-break galaxies at $z \sim 2-4$ (Steidel et al. 2018; Begley et al. 2022; Pahl et al. 2023), measurements of $H\alpha$ should trace the intrinsic production of ionizing photons reasonably well. The value of ξ_{ion} can also be inferred from the strength of [OIII] + $H\beta$ emission; however, due to the dependence of [OIII] emission on metallicity and the ionization parameter, the correlation is not as tight as with $H\alpha$ (e.g., Chevillard et al. 2018).

Previous work at $z \lesssim 2.5$, where direct $H\alpha$ spectroscopy has been possible from the ground, has found a mean $\log_{10} \xi_{\text{ion}}$ [erg Hz^{-1}] ≈ 25.3 , with a scatter of ~ 0.3 dex, likely dominated by variations in stellar populations between galaxies (e.g., Shivaei et al. 2018; Tang et al. 2019). At higher redshifts, where $H\alpha$ redshifts into the infrared, broadband photometry with *Spitzer* has been used extensively to estimate $H\alpha$ line fluxes (e.g., Schaerer & de Barros 2009; Shim et al. 2011; Stark et al. 2013; Smit et al. 2015; Bouwens et al. 2016; Lam et al. 2019; Maseda et al. 2020; Stefanon et al. 2022).

However, due to the limited spatial resolution and sensitivity of *Spitzer*, previous works were limited to studying ξ_{ion} in isolated, bright ($>L^*$) galaxies, where de-blending Infrared Array Camera (IRAC) photometry was possible (e.g., Bouwens et al. 2016), and using stacks for fainter galaxies (e.g., Lam et al. 2019; Maseda et al. 2020). With *James Webb* Space Telescope (JWST) it is finally possible to extend these studies to individual UV-faint galaxies (Endsley et al. 2022) and obtain rest-frame optical spectroscopy at $z > 3$ (e.g., Sun et al. 2022; Williams et al. 2022).

Results from previous analyses have been intriguing but require further investigation. Using stacked IRAC photometry, Lam et al. (2019) find no significant evidence for a strong cor-

relation of ξ_{ion} with M_{UV} . However, Maseda et al. (2020) find a population of extremely UV-faint galaxies ($M_{\text{UV}} > -16$) selected as $\text{Ly}\alpha$ emitters in deep Multi Unit Spectroscopic Explorer (MUSE) observations, which have very elevated ξ_{ion} compared to higher luminosity galaxies and at fixed $H\alpha$ equivalent widths (EWs), which implies that these efficient ionizing galaxies are particularly young and of low metallicity. It is thus important to examine the distribution of ξ_{ion} at low UV luminosities, and to compare galaxies with and without $\text{Ly}\alpha$ emission to better understand the demographics of the ionizing population.

Furthermore, using early JWST NIRCcam data, Endsley et al. (2022) discovered a population of UV-faint galaxies ($M_{\text{UV}} \sim -19$) at $z \sim 6.5-8$ with high specific star formation rates (sSFRs) but low EW [OIII]+ $H\beta$ inferred from photometry. The high sSFR would imply high ξ_{ion} due to the increased abundance of O and B stars. To explain the low [OIII]+ $H\beta$ EW, Endsley et al. (2022) suggest that either these galaxies have extremely low metallicities (reducing oxygen abundance) or, alternatively, that all nebular lines are reduced. A reduction in all nebular lines could be due to either them being produced in density-bounded HII regions with a very high ionizing escape fraction (e.g. Zackrisson et al. 2013; Marques-Chaves & Schaerer 2022) or a recent cessation of star formation. At $z \sim 3-7$, both [OIII]+ $H\beta$ and $H\alpha$ are visible in NIRCcam photometry, enabling us to test these scenarios.

In this paper we make use of deep multiband *Hubble* Space Telescope (HST)/ACS, WFC3, and JWST/NIRCcam imaging with overlapping MUSE observations, which enables us to blindly detect a spectroscopic sample with precision rest-frame UV-to-optical photometry. We measure the distribution of ξ_{ion} over a broader luminosity range ($-23 \lesssim M_{\text{UV}} \lesssim -15.5$) than previously possible in individual galaxies thanks to the excellent resolution and sensitivity of NIRCcam at rest-optical wavelengths compared to *Spitzer*/IRAC as well as the power of gravitational lensing. We explore correlations of ξ_{ion} with empirical galaxy properties. We find significant trends of increasing ξ_{ion} with decreasing UV luminosity, decreasing UV β slope, and increasing $H\alpha$ EW, all of which implies that the strongest ionizers are young sources with expected low metallicities. We also explore whether our sample shows evidence for very low metallicities or an extremely high escape fraction.

The paper is structured as follows. In Sect. 2 we describe the photometric and spectroscopic data for our study. In Sect. 3 we describe how we infer the ionizing production rate, ξ_{ion} , and in Sect. 4 we describe the correlations we find between ξ_{ion} and other galaxy properties and present a comparison to the literature. We discuss our results and state our conclusions in Sect. 6.

We assume a flat Λ cold dark matter cosmology with $\Omega_m = 0.3$, $\Omega_\Lambda = 0.7$ and $h = 0.7$. All magnitudes are in the AB system.

2. Data

For this work we selected fields with multiband HST/ACS and JWST/NIRCcam imaging and overlapping MUSE spectroscopy. We selected sources detected with $\text{Ly}\alpha$ emission ($z \sim 2.9-6.7$ in MUSE) and sources with a high probability of being in the same redshift range based on photometric redshift, and we used the HST + JWST photometry to extract optical emission line fluxes. Below we describe the data sets and the selection of our sample.

2.1. Imaging

We used JWST NIRCcam imaging in parallel to and of the cluster Abell 2744 from the GLASS-JWST program ERS-1324 (PI

Treu; Treu et al. 2022) and the UNCOVER¹ program GO-2561 (co-PIs Labbé and Bezanson).

The GLASS-JWST NIRC*am* observations discussed in this paper were taken in parallel to NIRISS observations of the cluster Abell 2744 on June 28–29, 2022. They are centered at RA = 3.5017025 deg and Dec = -30.3375436 deg and consist of imaging in seven bands: *F090W* (total exposure time: 11 520 s), *F115W* (11 520 s.), *F150W* (6120 s.), *F200W* (5400 s.), *F277W* (5400 s.), *F356W* (6120 s.), and *F444W* (23400 s.). The UNCOVER NIRC*am* observations of the Abell 2744 cluster were taken on November 2–15, 2022. They are centered at RA = 3.5760475 deg and Dec = -30.37946 deg and consist of imaging in seven bands: *F115W* (10823 s.), *F150W* (10823 s.), *F200W* (6700 s.), *F277W* (6700 s.), *F356W* (6700 s.), *F410M* (6700 s.), and *F444W* (8246 s.).

In our analysis, we also included new and archival HST imaging; the ACS imaging is particularly important for constraining photometric redshifts. This includes new HST/ACS data in *F606W* (59 530 s.), *F775W* (23 550 s.), and *F814W* (123 920 s) from HST-GO/DD program 17231² (PI Treu), as well as archival data acquired under the *Hubble* Frontier Fields program (HST-GO/DD-13495, PI Lotz; Lotz et al. 2017), BUFFALO (HST-GO-15117 PI Steinhardt; Steinhardt et al. 2020), and programs HST-GO-11689 (PI Dupke), HST-GO-11386 (PI Rodney), HST-GO-13389 (PI Siana), HST-GO-15940 (PI Ribeiro), and HST-SNAP-16729 (PI Kelly). Not all HST bands cover every object in our sample, and we only kept objects in our sample that have a well-constrained photometric redshift, usually meaning that there is ACS coverage (see Sect. 2.4). We also included HST/WFC3 imaging for completeness, but it is generally not as constraining as the NIRC*am* fluxes.

The image reduction and calibration, and the methods used to detect sources and measure multiband photometry in both fields, closely follow that of Brammer et al. (in prep.). Briefly, we pulled calibrated images from the Mikulski Archive for Space Telescopes (MAST)³ and processed them with the *grizli* pipeline (Brammer et al. 2022). The pipeline first aligns the exposures to external catalogs and to one another and corrects for any distortion within the image. Following this, we subtracted a sky-level background, divided out flat-field structure using custom flat-field images, and corrected for $1/f$ noise. We also corrected for NIRC*am* image anomalies, which include persistence, any remaining cosmic rays, and “snowballs” (see Rigby et al. 2023). Finally, we applied zero-point corrections calculated by G. Brammer⁴ and drizzled all exposures to a common pixel grid.

For source detection, we used SEP, Source Extraction and Photometry (Barbary 2018), to perform aperture photometry on the *F444W* detection image in each field.

2.2. VLT/MUSE spectroscopy

MUSE spectroscopy of the Abell 2744 cluster was obtained through ESO program 094.A-0115 (PI Richard) and is described by Mahler et al. (2018) and Richard et al. (2021). We used their publicly available catalog to select Ly α -emitting galaxies. The data comprise a 4 sq. arcmin mosaic centered on the cluster core. Four 1 sq. arcmin quadrants were observed for a total of 3.5, 4, 4,

and 5 h, respectively, and the center of the cluster was observed for an additional 2 h. The median line flux 1σ uncertainty in the MUSE data is 3.6×10^{-19} erg s⁻¹ cm⁻². This corresponds to a 5σ EW limit of $\sim 4\text{--}30$ Å over $z \sim 3\text{--}7$ for a galaxy with $M_{UV} = -19$ (the median for our sample before accounting for magnification as EW is invariant under magnification).

Very Large Telescope (VLT)/MUSE spectroscopy in the GLASS-JWST NIRC*am* fields were obtained through a new ESO Director’s Discretionary Time program, 109.24EZ.001 (co-PIs Mason, Vanzella), on the nights of July 28 and August 20, 2022. The data comprise five pointings (four of which are over 4 sq. arcmin and overlap with NIRC*am* imaging), each with 1 h of exposure time. The raw data are publicly available on the ESO archive⁵. The reduction, calibration, and source detection methods used for this work are identical to techniques described in Caminha et al. (2017, 2019). A full assessment of the depth is ongoing, but, based on the ~ 4 h depth of the Mahler et al. (2018) observations described above, we estimate a 5σ EW limit of $\sim 8\text{--}60$ Å in these shallower data.

In this work we used 102 spectroscopic confirmations at $z \sim 2.9\text{--}6.7$: 42 from the GLASS-JWST NIRC*am* fields and 60 from the Abell 2744 cluster field.

2.3. Gravitational lensing magnification

For the galaxies detected in the core of the Abell 2744 cluster, we corrected for gravitational lensing magnification using the model from Bergamini et al. (2023). The median magnification of the sample is $\mu = 3.54$, and 90% of the galaxies have $\mu = 2\text{--}20$. We removed sources with a magnification with $\mu > 50$ (12 sources) due to high uncertainties in the model near the critical curves. The galaxies in the parallel fields are $\sim 3\text{--}10'$ away from the cluster core, where the magnification is expected to be modest ($\mu \approx 1$). We do not account for the magnification of these sources.

2.4. Sample selection

For this work we focused on selecting a sample of galaxies at $z \sim 3\text{--}7$ with high purity. We selected 102 MUSE Ly α -detected galaxies with overlapping HST/ACS and JWST/NIRC*am* data as described above. We also selected a comparison sample of galaxies based on peak photometric redshift, within the same footprint as the MUSE observations, which we expect to have slightly lower H α EWs than the Ly α -selected sample.

We found the photometric redshift distribution of all sources detected as described in Sect. 2.1 using EAZY (Brammer et al. 2008) and using all available photometric bands. To build a photometric sample with high purity, following Bouwens et al. (2016), we selected sources with the peak of their photometric redshift between $2.9 < z < 6.7$ and kept only sources that have 90% of the redshift probability density between $\Delta z \sim 1$ of the peak of their distribution. The resulting high purity photometric sample consists of 268 galaxies.

The redshift and UV magnitude distribution of our sample is shown in Fig. 1. The median redshift of the full sample is 4.02, and the Ly α -selected sample has a median redshift of 3.95. The median M_{UV} is -18.1 , with a Kolmogorov-Smirnov (KS) test showing no significant difference between the Ly α - and photometrically selected samples.

¹ <https://www.stsci.edu/jwst/science-execution/program-information.html?id=2561>

² <https://www.stsci.edu/cgi-bin/get-proposal-info?id=17231&observatory=HST>

³ <https://archive.stsci.edu>

⁴ <https://github.com/gbrammer/grizli/pull/107>

⁵ http://archive.eso.org/wdb/wdb/eso/sched_rep_arc/query?progid=109.24EZ.001

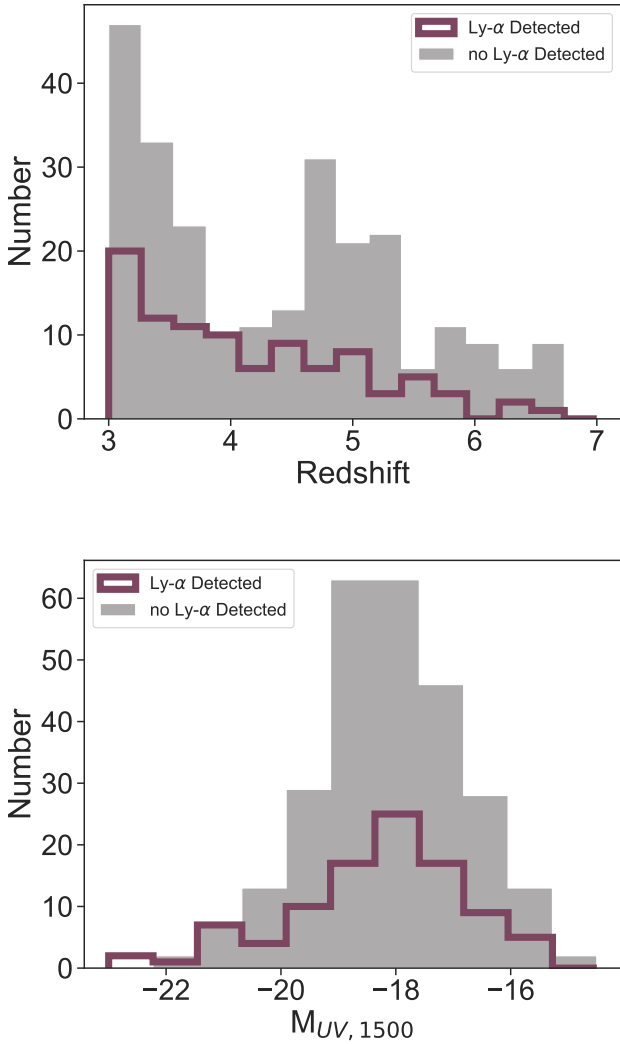


Fig. 1. Galaxies studied in this work: Ly α -detected galaxies (in purple) and galaxies photometrically selected (with no Ly α -detected, in gray). Top: Distribution of redshifts for the spectroscopic and photometric samples. We show the spectroscopic redshift, where available, or the peak photometric redshift. Bottom: UV magnitude distribution for our sample. We find a median value of -18.14 ± 1.58 , with no statistically significant difference between the two samples.

3. Inferring the ionizing photon production rate

3.1. Inferring nebular emission line strengths from photometry

To estimate nebular emission line fluxes from broadband photometry, we followed approaches in the literature and fit the spectral energy distribution (SED) to the full photometry, excluding bands we expected to contain strong nebular emission lines (e.g., Shim et al. 2011; Stark et al. 2013; Marmol-Queralto et al. 2016; Bouwens et al. 2016). This provided us with a model for the continuum flux in those bands that we could subtract from the observed photometry to infer the line flux.

We used BAGPIPES to fit SEDs (Carnall et al. 2018). We adopted BC03 (Bruzual & Charlot 2003) templates and excluded any nebular emission contribution. We did not consider any broadbands where H α or [OIII] + H β are observed according to each galaxy’s redshift. For ease of comparison to the literature (e.g., Maseda et al. 2020; Lam et al. 2019), we assumed

a Chabrier (2003) initial mass function and a Small Magellanic Cloud (SMC; Prevot et al. 1984) dust attenuation law, allowing A_V to vary from 0–3 mag. Because metallicity is not well known at the range of redshifts we explored, we allowed metallicity to vary from 0–2 Z_\odot . And because star formation histories are notoriously difficult to constrain at high redshifts (Strait et al. 2021), we assumed an exponentially rising delayed τ star formation history, allowing τ to vary freely. For the spectroscopically confirmed Lyman α emitters, we fixed the redshift at the Ly α redshift. For our photometric sample, we used the photometric redshift obtained from EAZY with a uniform prior with $\Delta z = 1$ (see Sect. 2.4).

We then compared the SED model of the galaxy’s continuum to the broadbands where H α or [OIII] + H β fall. We multiplied the non-nebular SED posteriors by the transmission of the aforementioned broadbands to obtain the contribution of the galaxy’s continuum to the observed flux. By subtracting this continuum flux contribution from the observed photometry, we were then able to recover the flux distributions of the H α and [OIII] + H β emission lines for each galaxy. We compared our measurements with a sample of six galaxies with [OIII] + H β EW measurements from the GLASS-ERS program using JWST/NIRISS (Boyett et al. 2022a), finding that our method recovers the EW of these sources to within ~ 20 –40%. A full comparison of these photometric inference methods is left to future work.

There are some limitations to our method for obtaining line fluxes, such as contamination from the 4000 Å break in the broadband that contains [OIII] + H β , the chance that the line falls outside the effective width of any of our broadband filters, or H α and [OIII] + H β falling on the same band. We considered a contribution of 6.8% from [NII] to the calculated H α flux, and 9.5% from [SII] according to Anders (2003). We removed galaxies with a poor χ^2 score (>50) on their SED fit; we chose this value by ignoring all galaxies on the high end of the χ^2 distribution.

The advantage of this approach, unlike estimating line fluxes directly from the SED fitting, is that it does not depend strongly on star formation history assumptions and allows us to make a mostly empirical measurement of the line fluxes. We obtain comparable results using the flux in the band redward of H α as the continuum flux, assuming a flat optical continuum (see also, e.g., Maseda et al. 2020). Estimating other physical parameters, such as the star formation rate and stellar mass, from the SED fitting did not give reliable results. This is because the fitting was too dependent on the initial assumptions and needed extremely young ages (<10 Myrs) and an instantaneous burst of star formation to recreate the observed nebular emissions.

The following results consist of 83 and 64 Ly α -emitting galaxies with H α and [OIII] + H β emission line measurements, respectively, and a photometric sample of 220 and 203 galaxies with H α and [OIII] + H β emission line measurements, respectively. We see both lines in 62 Ly α galaxies and 177 photometrically selected galaxies. We see no apparent biases in our M_{UV} distribution after narrowing down the sample. Nebular emission flux errors are derived from the 68% confidence interval of the resulting distributions.

3.2. Measuring UV absolute magnitude and slope

To infer the UV absolute magnitude, M_{UV} (magnitude at 1500 Å), and β slope, we fit the power law (e.g., Rogers et al. 2013) $f_\lambda \propto \lambda^\beta$ to the fluxes from the HST and JWST bands. We performed the fit using a Markov chain Monte Carlo sampling and the python module emcee (Foreman-Mackey et al. 2013).

Table 1. Linear fitting parameters for trends with $\log_{10}(1 - f_{\text{esc}})\xi_{\text{ion}}$.

Parameter	Slope, α	Intercept, β	Scatter variance, σ_{ϵ}^2
$M_{\text{UV}} + 20$	0.03 ± 0.02	25.33 ± 0.03	0.027 ± 0.006
$\log_{10} \text{EW}_{\text{H}\alpha} - 2.5$	0.73 ± 0.04	25.14 ± 0.02	0.003 ± 0.001
$\beta + 2$	-0.20 ± 0.04	25.38 ± 0.01	0.032 ± 0.005

Notes. We fit for $\log_{10}[(1 - f_{\text{esc}})\xi_{\text{ion}}] = \alpha + \beta X + \epsilon$, where ϵ is the intrinsic scatter and is assumed to be normally distributed with variance σ_{ϵ}^2 .

We assumed flat priors for β and M_{UV} , with bounds $-4 < \beta < 1$ and $-25 < M_{\text{UV}} < -12$, sufficient to explore the common value ranges for galaxies (e.g., Bouwens et al. 2014).

To obtain the photometric bands that are observing the UV rest frame of our galaxies, we excluded any bands that fall blueward of Lyman- α and might be affected by the Lyman break. For the same reason, we excluded bands redward of the 4000 Å break in the rest frame. After these requirements, we are left with three or four bands for each source. In the case of galaxies with Lyman- α detected in MUSE, we used the line's redshift. For photometrically selected galaxies, in each call of the likelihood, we randomly drew a redshift from a Normal distribution, $N(\mu = z_{\text{phot}}, \sigma = 0.5)$, and selected the appropriate photometric bands. For lensed sources, we considered magnifications and applied them following the same random draw method as for the redshift. We used the corresponding magnification and error obtained from the Bergamini et al. (2023) lensing model.

3.3. Determination of ξ_{ion}

We defined the production rate of ionizing photons, ξ_{ion} , as the ratio between the luminosity of observed ionizing photons and the intrinsic luminosity of the ionizing UV photons (e.g., Leitherer & Heckman 1995):

$$\xi_{\text{ion}} = \frac{L_{\text{H}\alpha}}{(1 - f_{\text{esc}})L_{\text{UV},\nu}^{\text{intr}}} \times 7.37 \times 10^{11} \text{ Hz erg}^{-1} \quad (1)$$

where $L_{\text{H}\alpha}$ is the unattenuated H α luminosity in erg s^{-1} and $L_{\nu,\text{UV},\text{intr}}$ is the intrinsic UV luminosity density at 1500 Å. The models from where the conversion factor is derived assume a young population of massive stars equivalent to a massive HII region. We assumed this type of environment to be similar to what we would find in young galaxies.

Because H α is produced by the excitation of hydrogen gas from ionizing radiation that does not escape the galaxy, and because we cannot directly measure f_{esc} in our sample, we note that the production rate we obtain is for ionizing photons that did not escape the galaxy, $\xi_{\text{ion}}(1 - f_{\text{esc}})$.

We first calculated $L_{\text{H}\alpha}$ directly from the SED obtained in Sect. 3.1, after accounting for dust attenuation (Prevot et al. 1984). To obtain the intrinsic value of the UV luminosity, we took the dust attenuation into account following Lam et al. (2019), who defined the intrinsic UV luminosity as $L_{\text{UV},\nu}^{\text{intr}} = L_{\text{UV},\nu}/f_{\text{esc,UV}}$, where $f_{\text{esc,UV}}$ is the fraction of escaping UV photons not absorbed by the dust. For this, we used the SMC dust law defined by Prevot et al. (1984):

$$f_{\text{esc,UV}} = 10^{-1.1(\beta+2.23)/2.5}, \quad \beta > -2.23 \quad (2)$$

where β is the UV slope obtained in Sect. 3.2. Galaxies with slopes bluer than $\beta < -2.23$ were assumed to be dust-free and therefore not corrected for dust.

In the following, uncertainties on ξ_{ion} are at the 68% confidence intervals and were obtained from propagating the uncertainty in the H α flux from its resulting distribution, as described in Sect. 3.1. The posterior distributions for β and M_{UV} were obtained as described in Sect. 3.2.

3.4. Correlation analysis

For the purpose of studying the correlations between galaxy properties, we used the python package `linmix`⁶ to perform Bayesian linear regression, including intrinsic scatter and accounting for two-dimensional errors (Kelly 2007). We fit for $\log_{10}[(1 - f_{\text{esc}})\xi_{\text{ion}}] = \alpha + \beta X + \epsilon$, where ϵ is the intrinsic scatter and is assumed to be normally distributed with a variance of σ_{ϵ}^2 . We recovered the best-fit trend line from the posteriors as well the 68% confidence interval on the parameters. We report the results in Table 1 and show the best-fit line in the figure plots.

4. Results

In this section we present our results. In Sect. 4.1 we study the trends between ξ_{ion} , H α EW, M_{UV} , and the β slope, and in Sect. 4.2 we investigate whether our sample shows evidence for galaxies with very high ionizing photon escape fractions and/or very low metallicities.

4.1. Behavior of ξ_{ion}

Figure 2 shows the distribution of $(1 - f_{\text{esc}})\xi_{\text{ion}}$ for our Ly α -selected and photometric samples. We find median values of $\log_{10} \xi_{\text{ion}}$ 25.39 ± 0.64 and 25.31 ± 0.43 , respectively, and 25.33 ± 0.47 [Hz erg^{-1}] for the complete data set. We find an intrinsic scatter of 0.42 dex, obtained by subtracting in quadrature the average uncertainty in $\log_{10} \xi_{\text{ion}}$ ($= 0.21$ dex) from the standard deviation of the observed distribution. The recovered intrinsic scatter is broader by ~ 0.1 dex than that found by Bouwens et al. (2016) and Shivaie et al. (2018) in $M_{\text{UV}} \lesssim -20$ galaxies. The broad distribution of ξ_{ion} is likely an outcome of the broad range of stellar populations in these galaxies, that is to say, due to a range of star formation histories (and thus ages) and stellar metallicities (see e.g., Shivaie et al. 2018).

We performed a two-sample KS test to determine whether the Ly α -selected and photometric samples are drawn from the same distribution. We recover a p-value of 0.03, meaning it is likely that the underlying distributions are different; this is consistent with the results from Saldana-Lopez et al. (2022), where a statistically significant difference is found between the ξ_{ion} distributions of Ly α emitters and non-Ly α emitters at $z \sim 3-5$. Given that galaxies with strong Ly α emission also likely have high ionizing photon escape fractions (e.g., Verhamme et al. 2015; Dijkstra et al. 2016), it is likely that the intrinsic

⁶ <https://github.com/jmeyers314/linmix>

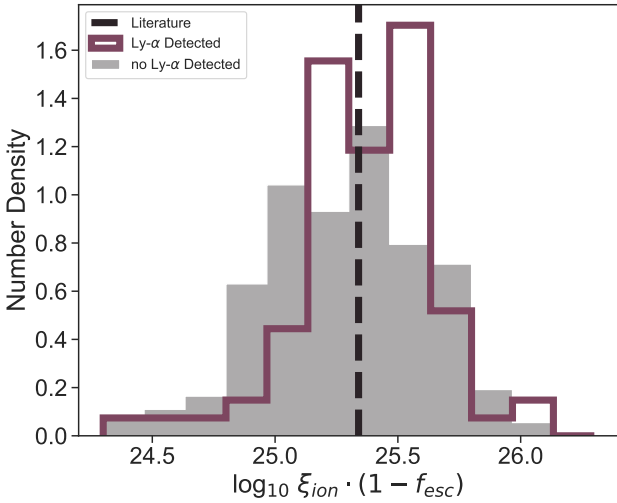


Fig. 2. Distribution of $(1 - f_{\text{esc}})\xi_{\text{ion}}$. The purple histogram includes galaxies with Ly α emission detection and the gray, galaxies without. Overall, Ly α -emitting galaxies show stronger ionizing photon production than galaxies with no Ly α emission, with median values 25.39 ± 0.64 and 25.31 ± 0.43 , respectively. We show the median relation from the literature at $z \sim 2-5$ as a dashed black line (e.g., Shivaei et al. 2018; Bouwens et al. 2016; Lam et al. 2019).

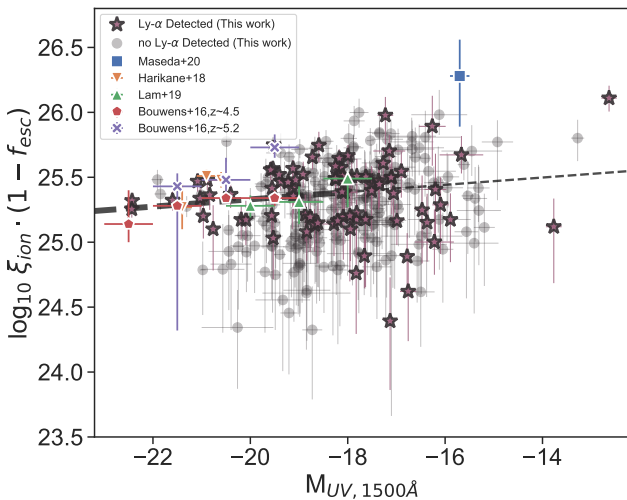


Fig. 3. M_{UV} vs. $(1 - f_{\text{esc}})\xi_{\text{ion}}$. Ly α -detected galaxies are shown with purple stars and photometrically selected sample with no Ly α -detected with gray circles. We show data from Maseda et al. (2020), Harikane et al. (2018), Lam et al. (2019), and Bouwens et al. (2016) as colored boxes for comparison. We find evidence for an increase in $\log_{10}(1 - f_{\text{esc}})\xi_{\text{ion}}$ toward fainter UV magnitudes, with a slope of 0.03 ± 0.02 , but only when considering the range where our sample is M_{UV} complete ($M_{\text{UV}} < -18.1$). We show literature constraints at similar redshifts as colored shapes (Bouwens et al. 2016; Harikane et al. 2018; Lam et al. 2019; Maseda et al. 2020), noting that all constraints fainter than $M_{\text{UV}} \gtrsim -20$ were obtained by stacking IRAC photometry.

ionizing photon production efficiency of these galaxies is even higher than what we can infer based on H α emission.

Figure 3 shows $(1 - f_{\text{esc}})\xi_{\text{ion}}$ versus UV magnitude and demonstrates the revolutionary capabilities of MUSE and JWST/NIRCam: we are able to spectroscopically confirm extremely UV-faint galaxies via their high Ly α EW, and we are able to infer H α , and therefore ξ_{ion} , from much fainter individual galaxies than was previously possible with *Spitzer*, where

stacking was necessary at $M_{\text{UV}} \gtrsim -20$ (e.g., Lam et al. 2019; Maseda et al. 2020). We reach ~ 1 dex lower than any previous studies at similar redshifts and without needing to use stacking methods. We can reach individual detections of very faint galaxies, $M_{\text{UV}} < -17$. We also find results consistent with those at $z \sim 2$ (Shivaei et al. 2018) and at $z \sim 4-5$ for $>L^*$ galaxies (Bouwens et al. 2016) and $<L^*$ galaxies (Lam et al. 2019, where a stacking analysis was used), as shown in Fig. 2. We note that our observations demonstrate the large scatter in $(1 - f_{\text{esc}})\xi_{\text{ion}}$ at fixed M_{UV} , which was not possible to observe in previous analyses that used the stacking of *Spitzer* photometry for UV-faint galaxies.

As described in Sect. 3.4, we performed a linear regression to assess correlations in our data. In contrast to Lam et al. (2019), we find significant evidence for a weak trend between ξ_{ion} and M_{UV} , where the highest ξ_{ion} tends to come from the faintest galaxies. Since our sample is not M_{UV} complete, we only study the correlation up to the peak of our M_{UV} distribution ($= -18.14$) in Fig. 1. We find $\log_{10}[(1 - f_{\text{esc}})\xi_{\text{ion}}] = (0.03 \pm 0.02)(M_{\text{UV}} + 20) + 25.36 \pm 0.03$, but with a large scatter (see Table 1).

Figure 4 shows that ξ_{ion} follows a strong trend with H α EW, as found in previous work (Harikane et al. 2018; Lam et al. 2019; Tang et al. 2019). Such works were limited to the highest H α EW values, while we reach ~ 0.75 dex lower due to the sensitivity of NIRCam. This trend is consistent with a picture where ξ_{ion} is elevated in the youngest, most highly star-forming galaxies (e.g., Tang et al. 2019). We find $\log_{10}[(1 - f_{\text{esc}})\xi_{\text{ion}}] = (0.73 \pm 0.04)(\log_{10} \text{EW}_{\text{H}\alpha} - 2.5) + 25.15 \pm 0.02$. The measurement by Maseda et al. (2020), obtained from a stack of extremely UV-faint galaxies with high Ly α EWs, lies significantly above our sample and values from the rest of the literature, with higher $(1 - f_{\text{esc}})\xi_{\text{ion}}$ at fixed H α EWs. As discussed by Maseda et al. (2020), this likely implies their sources have a much lower gas-phase metallicity than other samples.

We also find that Ly α -selected galaxies have a higher H α EW than the photometrically selected sample (median EW = $732 \pm 187 \text{ \AA}$ compared to $457 \pm 161 \text{ \AA}$ for the photometric sample). A two-sample KS test establishes that the EW distributions of the two samples are different (p -value $\ll 0.01$). This is likely the primary driver of the increased ξ_{ion} distribution for the Ly α -selected sample (Fig. 2).

At a fixed H α EW, we see a clear tendency for galaxies with very blue β UV slopes to have elevated ξ_{ion} (Fig. 4). This trend is also seen in the full sample (Fig. 5), where we find high ξ_{ion} is weakly correlated to a blue β slope, but with a large scatter. We find $\log_{10}(1 - f_{\text{esc}})\xi_{\text{ion}} = (-0.20 \pm 0.04)(\beta + 2) + 25.41 \pm 0.01$ (see Table 1). Similar correlations have been seen at $z \sim 6$ (e.g., Ning et al. 2023). Using a KS test, we find no significant difference in the β distributions for the Ly α and photometric samples. Our sample has a median $\beta = -2.1$.

4.2. A search for high-escape-fraction and extremely low-metallicity galaxies

As well as being a tracer of the ionizing photon production of galaxies, nebular emission lines are also sensitive to the escape fraction. Zackrisson et al. (2013) proposed that in galaxies with a very high ionizing escape fraction, one would expect a reduction in nebular emission line strength (H β EW $\lesssim 30 \text{ \AA}$) and extremely blue UV slopes ($\beta < -2.5$) due to the lack of nebular continuum. Early JWST observations have discovered potentially very blue galaxies (Topping et al. 2022, though cf. Cullen et al. 2023) and galaxies with weak nebular line emission yet high sSFRs (via [OIII] + H β ; Endsley et al. 2022), potentially indicating a

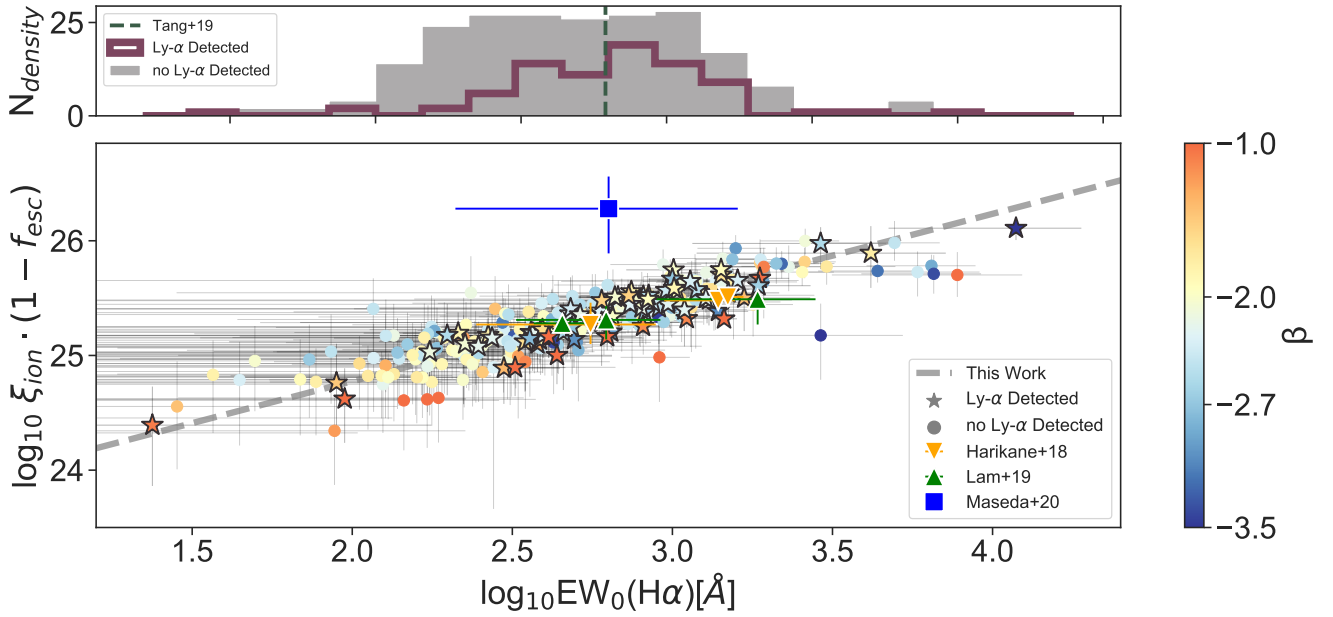


Fig. 4. Comparison of the $H\alpha$ EW with the ionizing photon production that does not escape the galaxy. $Ly\alpha$ -detected galaxies are shown as stars and photometrically selected galaxies with no $Ly\alpha$ as circles. As above, error bars are only shown for 30% of the sources for clarity. We color-code these two samples by UV β slope. In the top panel we show the distribution of $H\alpha$ EWs for the same two samples compared to the values found by Tang et al. (2019). We add data from Harikane et al. (2018) and Lam et al. (2019), which are at the high end of our observed $H\alpha$ EW distribution, for comparison. We see that a higher ξ_{ion} correlates very strongly with a higher $H\alpha$ EW. Galaxies with detected $Ly\alpha$ emission have an $H\alpha$ EW distribution with higher values, median $732 \pm 187 \text{ \AA}$ compared to $457 \pm 161 \text{ \AA}$ with a Kolmogorov-Smirnov test p -value $\ll 0.01$. The sources with the reddest UV slopes systematically lie below the best-fit relation at fixed $H\alpha$ EW.

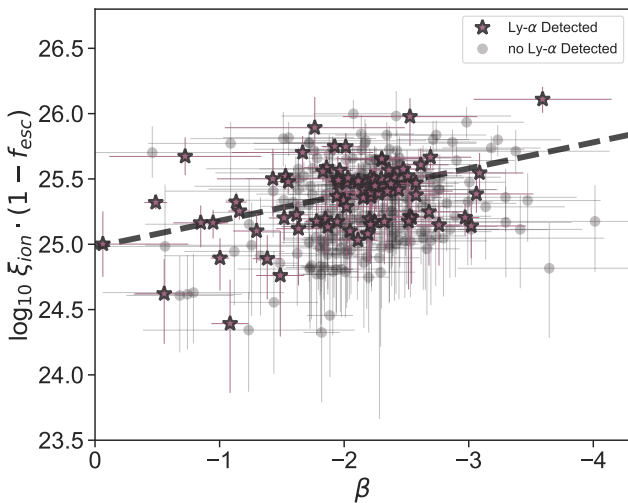


Fig. 5. UV β slope vs. $\xi_{ion}(1 - f_{esc})$. $Ly\alpha$ -detected galaxies are shown in purple and the photometrically selected sample with no $Ly\alpha$ -detected in gray. As above, error bars are only shown for 30% of the sources for clarity. We add the stacked measurements from Lam et al. (2019) for comparison. We find a very weak trend of increasing ξ_{ion} with decreasing β , with a linear slope of -0.10 ± 0.06 .

population with a high ionizing escape fraction. However, the observation of low $[OIII] + H\beta$ line strengths could also be caused by very low gas-phase metallicity (decreasing the strength of $[OIII]$ emission) or a recent turnoff in star formation (which would also decrease all nebular emission lines). Given the redshift range of our sample, we can infer both $H\alpha$ and $[OIII] + H\beta$ line strengths for 241 galaxies, allowing us to test these scenarios and to search for galaxies with a high escape

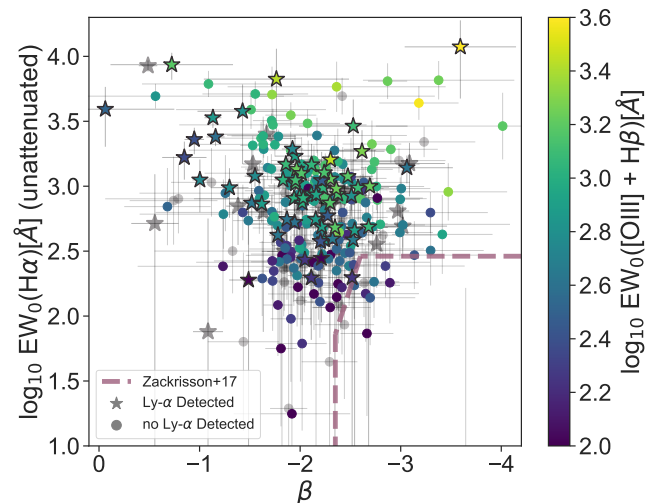


Fig. 6. Comparison between the intrinsic (unattenuated) EW of $H\alpha$ and the UV β slope, color-coded by $[OIII] + H\beta$ EW. $Ly\alpha$ galaxies are shown with star-shaped markers, and the photometric sample as circles. Galaxies shown in gray do not have $[OIII] + H\beta$ EW measurements. We show the region predicted by Zackrisson et al. (2017) to show $f_{esc} > 0.5$. We rescale from $H\beta$ EW to intrinsic $H\alpha$ with a case B recombination scenario of factor 2.89, assuming a flat optical continuum in f_{λ} , which we confirm from the SED fitting done in Sect. 3.1.

fraction. We obtained the $[OIII] + H\beta$ nebular line fluxes as described in Sect. 3.1.

In Fig. 6 we show UV β slopes as a function of intrinsic $H\alpha$ EW for our sample (where we correct for dust attenuation as described in Sect. 3.1). We compare our sample to the region proposed by Zackrisson et al. (2017) to have $f_{esc} >$

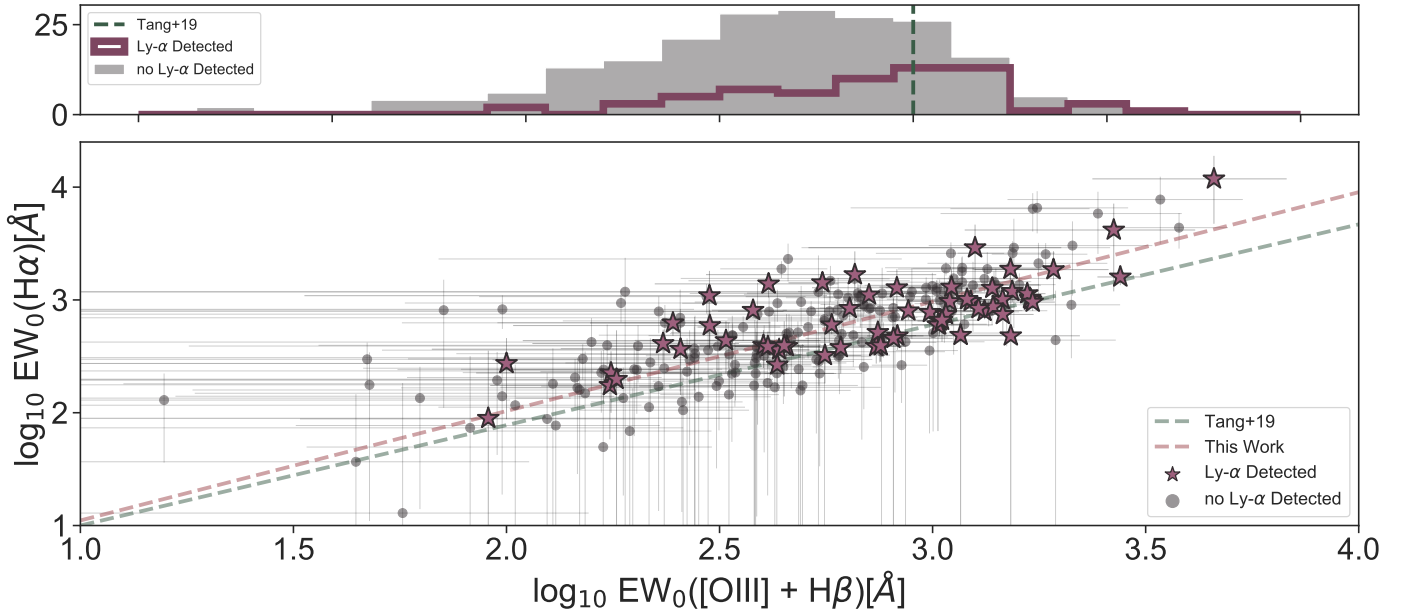


Fig. 7. Comparison between the EW of $H\alpha$ and $[OIII] + H\beta$. $Ly\alpha$ -detected galaxies are shown as stars and the photometrically selected sample with no $Ly\alpha$ -detected as circles. In the top panel we show the distribution of $[OIII] + H\beta$ EW for both of our samples. We find a very strong correlation between $H\alpha$ EW and the $[OIII] + H\beta$ EW, though with large scatter. The dashed lines are the correlation trends found for this work (red) and Tang et al. (2019, green). The $H\alpha$ EW/ $[OIII] + H\beta$ EW is higher than the $z \sim 2$ sample from Tang et al. (2019), which was selected to have a strong $[OIII]$ EW, implying that we might be observing lower-metallicity galaxies.

0.5. While several sources fall into this region, and also have low $[OIII] + H\beta$ EWs ($\lesssim 100 \text{ \AA}$), the uncertainties are too large to make them robust candidates. We discuss this further in Sect. 5.2.

Figure 7 shows the $H\alpha$ EW as a function of $[OIII] + H\beta$ for our sample. We see the expected positive correlation between both nebular emission lines, as these lines are all generated by the effects of stellar ionizing radiation. We see a very large scatter (with a range of ~ 1.5 dex) as expected due to variations in metallicity, temperature, and the ionization parameter, all of which affect the strength of individual $[OIII]$ galaxies (e.g., Maiolino et al. 2008; Steidel et al. 2014; Sanders et al. 2021). We find $\log_{10} EW(H\alpha) = 0.97 \pm 0.06(\log_{10} EW([OIII] + H\beta) - 2.5) + 2.52 \pm 0.03$.

Galaxies with detected $Ly\alpha$ emission tend to occupy the top right of the plot, with strong nebular emission lines, suggesting they are young star-forming galaxies with low metallicities and large ionization parameters that produce these emission lines (see e.g., Yang et al. 2017; Du et al. 2020; Tang et al. 2021, for more detailed studies). We find the $Ly\alpha$ -selected galaxies have stronger $[OIII] + H\beta$ EWs compared to the photometric population, following the trend with $H\alpha$ EW in Fig. 4. However, as discussed by Tang et al. (2021), not all galaxies with strong nebular emission are detected in $Ly\alpha$, indicating that $Ly\alpha$ transmission is reduced due to a high column density of neutral gas in these systems and/or inclination effects. We compare our data to a $z \sim 2$ sample by Tang et al. (2019), which was selected based on strong $[OIII]$ emission. We find a similar correlation, but overall our ratio of $H\alpha$ EW/ $[OIII] + H\beta$ EW is higher by ~ 0.1 dex. Given that the Tang et al. (2019) sample has a significantly subsolar gas-phase metallicity, $Z < 0.3Z_{\odot}$ (Tang et al. 2021), the decrease we observe in $[OIII]$ at fixed $H\alpha$ EW would likely imply an overall lower metallicity due to a lower number of metal atoms in our sample.

5. Discussion

5.1. The profile of a strong ionizer

Thanks to the depth of JWST/NIRCam, we have been able to assess trends of ξ_{ion} at $z > 3$ across the broadest range of galaxy properties to date. From these results, we corroborate previous work at lower redshifts and high luminosities and push the measurement of ξ_{ion} to a large sample of individual UV-faint galaxies for the first time.

We find that galaxies with strong ionizing photon emission tend to have high $H\alpha$ EWs, low UV luminosities, blue UV β slopes, and $Ly\alpha$ emission – all implying that these galaxies are young and likely have a low dust content, low metallicity, and a high O/B star population that is capable of producing hard ionizing photons (e.g., Tang et al. 2019; Boyett et al. 2022b). This picture of the integrated emission from galaxies is complemented by high spatial resolution observations of highly magnified arcs with JWST. They have revealed extremely young star clusters ($\lesssim 10$ Myr) with $[OIII] + H\beta$ EW $> 1000 \text{ \AA}$. They dominate the ionizing photon production in their galaxy (Vanzella et al. 2022, 2023), indicating that there can be large variations in ξ_{ion} in individual galaxies if they contain multiple stellar populations, but also that the variation is primarily driven by the age of the stellar populations. We also find that, overall, our $Ly\alpha$ galaxy sample has higher ξ_{ion} than the photometrically selected one; the primary reason for this difference is that the former has higher $H\alpha$ EWs (Fig. 4). The enhanced prevalence of $Ly\alpha$ emission in strong $H\alpha$ emitters is likely a combination of an increased production of $Ly\alpha$ photons due to the young stellar population implied by the strong $H\alpha$ and (potentially) an increase in the $Ly\alpha$ escape fraction in the ISM (Tang et al. 2021; Naidu et al. 2022). In these rapidly star-forming galaxies, the hard ionizing radiation may be ionizing the ISM and/or feedback may disrupt the ISM gas, leading to a reduced HI column density and dust cover. We note that the galaxies with the

highest $(1 - f_{\text{esc}})\xi_{\text{ion}}$ are not necessarily all Ly α emitters, likely due to variance in the geometry and column density of neutral gas and dust in these sources. Ning et al. (2023) show this same correlation between ξ_{ion} and Ly α for a broad range of luminosities and EWs.

5.2. The ionizing photon escape fraction

In Sect. 4.2 we explore whether our sample shows signs of high ionizing photon escape fraction, f_{esc} , using the low H β EW–blue UV β slope region defined by Zackrisson et al. (2017) for $f_{\text{esc}} > 0.5$. While several sources fell into this region, with both low H α EW and [OIII] + H β EW ($\lesssim 100 \text{ \AA}$), the uncertainties on the line flux measurements are too large for them to be robust candidates. More precise emission line measurements with JWST spectroscopy will be vital for identifying such candidates and their relative abundance in the galaxy population.

The lack of high f_{esc} candidates amongst the Ly α -selected galaxies is also surprising. As the same conditions (a low neutral gas covering fraction) facilitate both Ly α escape and Lyman continuum escape, a correlation between the two is expected (e.g., Verhamme et al. 2015; Dijkstra et al. 2016; Reddy et al. 2016).

As discussed by Topping et al. (2022), however, it is possible for galaxies with high f_{esc} but very young ages to still have high nebular emission due to high ionizing photon production. It is likely that the criteria proposed by Zackrisson et al. (2017) can only find high f_{esc} systems within the bounds of the assumptions made for their model, such as galaxy star formation histories, ages, metallicities, and dust levels, but also the stellar models used. Our results suggest the low luminosity galaxies with high sSFRs but low [OIII] + H β EWs observed by Endsley et al. (2022) may be more likely due to variations in metallicity than due to the high f_{esc} .

6. Conclusions

We have inferred the hydrogen ionizing photon production rate, modulo the escape fraction, in the largest sample of individual sub- L^* $z > 3$ galaxies to date, spanning $-23 \lesssim M_{\text{UV}} \lesssim -15.5$ with a median $M_{\text{UV}} = -18.1$, thanks to deep JWST/NIRCam imaging. This has enabled us to track the demographics of the ionizing population. Our conclusions are as follows:

1. The median $\log_{10}(1 - f_{\text{esc}})\xi_{\text{ion}}$ of our sample is 25.33 ± 0.47 with an intrinsic scatter of 0.42 dex. The inferred ξ_{ion} distribution of our sample has values in a range of ~ 1.5 dex, implying a wide range of galaxy properties and ages.
2. We find significant trends of increasing $(1 - f_{\text{esc}})\xi_{\text{ion}}$ with increasing H α EW, decreasing UV luminosity, and decreasing UV slope, all suggesting that the galaxies most efficient at producing ionizing photons are young, highly star-forming, and normally expected to have low metallicities and be dust-poor.
3. We find galaxies selected with strong Ly α emission to have higher ξ_{ion} than photometrically selected galaxies, with median $\log_{10}(1 - f_{\text{esc}})\xi_{\text{ion}}$ values of 25.39 ± 0.64 and 25.31 ± 0.43 , respectively. We find the Ly α -detected galaxies have an elevated H α EW distribution, and thus the increased ξ_{ion} is likely driven by the selection based on Ly α selecting a younger population. As strong Ly α emitters also likely have high ionizing photon escape fractions, this implies the intrinsic production rate of ionizing photons in these galaxies could be significantly higher than what we can infer from H α luminosities.
4. We examine our sample for signs of very high f_{esc} by comparing the inferred strengths of nebular emission lines ([OIII] + H β and H α) and the strength of the nebular continuum via the UV β slope. We find no significant evidence for sources with high-escape-fraction galaxies with low nebular emission line strengths and very blue UV β slopes. The reduced strength of the [OIII] + H β EWs in our $z > 3$ sample compared to a sample at $z \sim 2$ from Tang et al. (2019) implies our sample likely has a lower gas-phase metallicity and/or ionization parameter.

We have demonstrated the power of JWST/NIRCam photometry to more precisely constrain the rest-frame optical emission of UV-faint high redshift galaxies than previously possible with *Spitzer*/IRAC. These observations allow us to constrain the production rate of ionizing photons from early galaxies, corroborating the picture obtained from previous stacking analyses, that ξ_{ion} is elevated in young, highly star-forming galaxies but that there is a broad distribution of ξ_{ion} , likely driven by variations in galaxy properties and ages.

With JWST spectroscopy it is becoming possible to obtain direct measurements of optical emission lines in large samples (e.g., Sun et al. 2022; Williams et al. 2022; Matthee et al. 2022). Deriving a census of the ionizing photon production rate across the full galaxy population will be necessary to fully understand reionization. Here we have shown that ξ_{ion} is elevated in UV-faint galaxies with strong nebular emission lines, likely due to young ages. While a thorough analysis of the implications of our results for reionization is beyond the scope of this work, it becomes more prominent at high redshift (e.g., Boyett et al. 2022b; Endsley et al. 2022), implying that it would be possible to complete reionization with modest f_{esc} . Considering the full distributions of ξ_{ion} and f_{esc} across galaxy properties will be required to assess the primary drivers of reionization.

Acknowledgements. We thank the co-PIs Ivo Labbé and Rachel Bezanson for the conception and public availability of the UNCOVER JWST Program (GO-2561), which made much of this work possible. We thank Mengtao Tang for sharing data the emission line catalog from Tang et al. (2019). This work is based on observations collected at the European Southern Observatory under ESO programmes 109.24EZ.001 and 094.A-0115. This work is based on NASA/ESA HST and JWST data which were obtained from the Mikulski Archive for Space Telescopes at the Space Telescope Science Institute, which is operated by the Association of Universities for Research in Astronomy, Inc., under NASA contract NAS 5-03127 for JWST. The HST observations are associated with programs GO/DD-17231, GO/DD-13495, GO-15117, GO-11689, GO-11386, GO-13389, GO-15940 and SNAP-16729. The JWST observations are associated with programs JWST-ERS-1324 and GO-2561. C.M. and G.P. acknowledge support by the VILLUM FONDEN under grant 37459. The Cosmic Dawn Center (DAWN) is funded by the Danish National Research Foundation under grant DNR140. We acknowledge financial support from NASA through grant JWST-ERS-1324. We acknowledge support from the INAF Large Grant 2022 “Extragalactic Surveys with JWST” (PI Pentericci), and support through grants PRIN-MIUR 2017WSCC32, 2020SKSTHZ. This research is supported in part by the Australian Research Council Centre of Excellence for All Sky Astrophysics in 3 Dimensions (ASTRO 3D), through project number CE170100013.

References

- Anders, P., & Fritze-v. Alvensleben, U., 2003, *A&A*, **401**, 1063
 Barbary, K. 2018, Astrophysics Source Code Library [record ascl:1811.004]
 Becker, G. D., D’Aloisio, A., Christenson, H. M., et al. 2021, *MNRAS*, **508**, 1853
 Begley, R., Cullen, F., McLure, R. J., et al. 2022, *MNRAS*, **513**, 3510
 Bergamini, P., Acebron, A., Grillo, C., et al. 2023, *A&A*, **670**, A60
 Bolan, P., Lemaux, B. C., Mason, C., et al. 2022, *MNRAS*, **517**, 3263
 Bouwens, R. J., Illingworth, G. D., Oesch, P. A., et al. 2014, *ApJ*, **793**, 115
 Bouwens, R. J., Smit, R., Labbé, I., et al. 2016, *ApJ*, **831**, 176
 Boyett, K., Mascia, S., Pentericci, L., et al. 2022a, *ApJ*, **940**, L52
 Boyett, K. N. K., Stark, D. P., Bunker, A. J., Tang, M., & Maseda, M. V. 2022b, *MNRAS*, **513**, 4451

- Brammer, G. B., van Dokkum, P. G., & Coppi, P. 2008, *ApJ*, **686**, 1503
- Brammer, G., Strait, V., Matharu, J., & Momcheva, I. 2022, <https://zenodo.org/record/6672538>
- Bruzual, G., & Charlot, S. 2003, *MNRAS*, **344**, 1000
- Caminha, G. B., Grillo, C., Rosati, P., et al. 2017, *A&A*, **600**, A90
- Caminha, G. B., Rosati, P., Grillo, C., et al. 2019, *A&A*, **632**, A36
- Carnall, A. C., McLure, R. J., Dunlop, J. S., & Davé, R. 2018, *MNRAS*, **480**, 4379
- Chabrier, G. 2003, *PASP*, **115**, 763
- Chevallard, J., Charlot, S., Senchyna, P., et al. 2018, *MNRAS*, **479**, 3264
- Cullen, F., McLure, R. J., McLeod, D. J., et al. 2023, *MNRAS*, **520**, 14
- Davies, F. B., Hennawi, J. F., Bañados, E., et al. 2018, *ApJ*, **864**, 142
- Dijkstra, M., Gronke, M., & Venkatesan, A. 2016, *ApJ*, **828**, 71
- Du, X., Shapley, A. E., Tang, M., et al. 2020, *ApJ*, **890**, 65
- Emami, N., Siana, B., Alavi, A., et al. 2020, *ApJ*, **895**, 116
- Endsley, R., Stark, D. P., Whittler, L., et al. 2022, ArXiv e-prints [arXiv:2208.14999]
- Fan, X., Strauss, M. A., Becker, R. H., et al. 2006, *AJ*, **132**, 117
- Foreman-Mackey, D., Hogg, D. W., Lang, D., & Goodman, J. 2013, *PASP*, **125**, 306
- Harikane, Y., Ouchi, M., Shibuya, T., et al. 2018, *ApJ*, **859**, 84
- Hashimoto, T., Laporte, N., Mawatari, K., et al. 2018, *Nature*, **557**, 392
- Inoue, A. K., Shimizu, I., Iwata, I., & Tanaka, M. 2014, *MNRAS*, **442**, 1805
- Kelly, B. C. 2007, *ApJ*, **665**, 1489
- Lam, D., Bouwens, R. J., Labbé, I., et al. 2019, *A&A*, **627**, A164
- Leitherer, C., & Heckman, T. M. 1995, *ApJS*, **96**, 9
- Lotz, J. M., Koekemoer, A., Coe, D., et al. 2017, *ApJ*, **837**, 97
- Ma, X., Quataert, E., Wetzel, A., et al. 2020, *MNRAS*, **498**, 2001
- Madau, P., Haardt, F., & Rees, M. J. 1999, *ApJ*, **514**, 648
- Mahler, G., Richard, J., Clément, B., et al. 2018, *MNRAS*, **473**, 663
- Maiolino, R., Nagao, T., Grazian, A., et al. 2008, *A&A*, **488**, 463
- Mármol-Queraltó, E., McLure, R. J., Cullen, F., et al. 2016, *MNRAS*, **460**, 3587
- Marques-Chaves, R., Schaerer, D., Álvarez-Márquez, J., et al. 2022, *MNRAS*, **517**, 2972
- Maseda, M. V., Bacon, R., Lam, D., et al. 2020, *MNRAS*, **493**, 5120
- Mason, C. A., Treu, T., Dijkstra, M., et al. 2018, *ApJ*, **856**, 2
- Mason, C. A., Fontana, A., Treu, T., et al. 2019, *MNRAS*, **485**, 3947
- Matthee, J., Mackenzie, R., Simcoe, R. A., et al. 2022, *ApJ*, submitted [arXiv:2211.08255]
- McGreer, I. D., Mesinger, A., & D'Odorico, V. 2015, *MNRAS*, **447**, 499
- McLeod, D. J., McLure, R. J., Dunlop, J. S., et al. 2021, *MNRAS*, **503**, 4413
- Naidu, R. P., Tacchella, S., Mason, C. A., et al. 2020, *ApJ*, **892**, 109
- Naidu, R. P., Matthee, J., Oesch, P. A., et al. 2022, *MNRAS*, **510**, 4582
- Ning, Y., Cai, Z., Jiang, L., et al. 2023, *ApJ*, **944**, L1
- Oesch, P. A., Bouwens, R. J., Illingworth, G. D., Labbe, I., & Stefanon, M. 2018, *ApJ*, **855**, 105
- Pahl, A. J., Shapley, A., Steidel, C. C., et al. 2023, *MNRAS*, **521**, 3247
- Planck Collaboration VI. 2020, *A&A*, **641**, A6
- Prevot, M. L., Lequeux, J., Maurice, E., Prevot, L., & Rocca-Volmerange, B. 1984, *A&A*, **132**, 389
- Qin, Y., Mesinger, A., Bosman, S. E. I., & Viel, M. 2021, *MNRAS*, **506**, 2390
- Reddy, N. A., Steidel, C. C., Pettini, M., Bogosavljević, M., & Shapley, A. E. 2016, *ApJ*, **828**, 108
- Richard, J., Claeysens, A., Lagattuta, D., et al. 2021, *A&A*, **646**, A83
- Rigby, J., Perrin, M., McElwain, M., et al. 2023, *PASP*, **135**, 048001
- Robertson, B. E., Ellis, R. S., Dunlop, J. S., McLure, R. J., & Stark, D. P. 2010, *Nature*, **468**, 49
- Rogers, A. B., McLure, R. J., & Dunlop, J. S. 2013, *MNRAS*, **429**, 2456
- Saldana-Lopez, A., Schaerer, D., Chisholm, J., et al. 2022, *MNRAS*, submitted [arXiv:2211.01351]
- Sanders, R. L., Shapley, A. E., Jones, T., et al. 2021, *ApJ*, **914**, 19
- Schaerer, D., & de Barros, S. 2009, *A&A*, **502**, 423
- Sharma, M., Theuns, T., Frenk, C., et al. 2017, *MNRAS*, **468**, 2176
- Shim, H., Chary, R.-R., Dickinson, M., et al. 2011, *ApJ*, **738**, 69
- Shivaei, I., Reddy, N. A., Siana, B., et al. 2018, *ApJ*, **855**, 42
- Smit, R., Bouwens, R. J., Franx, M., et al. 2015, *ApJ*, **801**, 122
- Stanway, E. R., Eldridge, J. J., & Becker, G. D. 2016, *MNRAS*, **456**, 485
- Stark, D. P., Ellis, R. S., Chiu, K., Ouchi, M., & Bunker, A. 2010, *MNRAS*, **408**, 1628
- Stark, D. P., Schenker, M. A., Ellis, R., et al. 2013, *ApJ*, **763**, 129
- Stefanon, M., Bouwens, R. J., Illingworth, G. D., et al. 2022, *ApJ*, **935**, 94
- Steidel, C. C., Rudie, G. C., Strom, A. L., et al. 2014, *ApJ*, **795**, 165
- Steidel, C. C., Bogosavljevic, M., Shapley, A. E., et al. 2018, *ApJ*, **869**, 123
- Steinhardt, C. L., Jauzac, M., Acebron, A., et al. 2020, *ApJS*, **247**, 64
- Strait, V., Bradač, M., Coe, D., et al. 2021, *ApJ*, **910**, 135
- Sun, F., Egami, E., Pirzkal, N., et al. 2022, *ApJ*, submitted [arXiv:2209.03374]
- Tang, M., Stark, D. P., Chevallard, J., & Charlot, S. 2019, *MNRAS*, **489**, 2572
- Tang, M., Stark, D. P., Chevallard, J., et al. 2021, *MNRAS*, **503**, 4105
- Topping, M. W., Stark, D. P., Endsley, R., et al. 2022, *ApJ*, **941**, 153
- Trebtsch, M., Blaizot, J., Rosdahl, J., Devriendt, J., & Slyz, A. 2017, *MNRAS*, **478**, 5607
- Treu, T., Roberts-Borsani, G., Bradac, M., et al. 2022, *ApJ*, **935**, 110
- Vanzella, E., Nonino, M., Cupani, G., et al. 2018, *MNRAS*, **476**, L15
- Vanzella, E., Castellano, M., Bergamini, P., et al. 2022, *ApJ*, **940**, L53
- Vanzella, E., Claeysens, A., Welch, B., et al. 2023, *ApJ*, **945**, 53
- Verhamme, A., Orlitová, I., Schaerer, D., & Hayes, M. 2015, *A&A*, **578**, A7
- Williams, H., Kelly, P. L., Chen, W., et al. 2022, ArXiv e-prints [arXiv:2210.15699]
- Yang, H., Malhotra, S., Rhoads, J. E., & Wang, J. 2017, *ApJ*, **847**, 38
- Zackrisson, E., Inoue, A. K., & Jensen, H. 2013, *ApJ*, **777**, 39
- Zackrisson, E., Binggeli, C., Finlator, K., et al. 2017, *ApJ*, **836**, 78